Post-print version of:

Title: **Multiaxial plain and notch fatigue strength of thick-walled ductile cast iron EN-GJS-600-3: Combining multiaxial fatigue criteria, theory of critical distances, and defect sensitivity**

Authors: **M. Benedetti, C. Santus, S. Raghavendra, D. Lusuardi, F. Zanini, S. Carmignato.**

Multiaxial plain and notch fatigue strength of thick-walled ductile cast iron EN-GJS-600-3:

Combining multiaxial fatigue criteria, theory of critical distances, and defect sensitivity

Matteo Benedetti[1*], Ciro Santus[2], Sunil Raghavendra[1], Danilo Lusuardi[3], Filippo Zanini[4], Simone Carmignato[4]

[1]*Department of Industrial Engineering, University of Trento, via Sommarive 9, 38123 Trento, Italy*

[2]*Department of Civil and Industrial Engineering, University of Pisa, Pisa, Italy*

[3]*Fonderie Ariotti, Adro (BS), Italy*

[4]*Department of Management and Engineering, University of Padua, Vicenza, Italy*

*Corresponding author

Matteo Benedetti

matteo.benedetti@unitn.it

Abstract

Multiaxial fatigue tests are carried out on plain and notched specimens extracted from EN-GJS-600-3 pearlitic DCI heavy-section castings. Two notches of different severities were combined for the determination of mode I and mode III critical distances, along with the related intrinsic fatigue strengths. SEM and CT clearly showed that fatigue cracks initiated from graphite nodules and shrinkage pores in notched and plain specimens, respectively. Different multiaxial criteria were compared, and best predictions obtained with the Carpinteri et al. criterion with four parameters: axial and torsional intrinsic fatigue strengths, combined with the two different related critical distances.

Keywords

Notch fatigue; Multiaxial fatigue; Defects; Theory of critical distances; Ductile cast iron

Nomenclature

$\sqrt{area}$	geometrical parameter of the defect
CT	computed tomography
D	notched specimen bar diameter
DCI	ductile cast iron
d_F	defect Feret diameter
HV	Vickers hardness
K_f	axial fatigue stress concentration factor

K_{fT}	torsional fatigue stress concentration factor
K_r	ratio of the axial fatigue stress concentration factors
K_{rT}	ratio of the torsional fatigue stress concentration factors
K_t	theoretical axial stress concentration factor
K_{tT}	theoretical torsional stress concentration factor
L^*	mode I critical length according to LM estimated from two notched specimen geometries
$L^{*'}$	mode I critical length according to PM estimated from two notched specimen geometries
L_T^*	mode III critical length according to LM estimated from two notched specimen geometries
$L_T^{*'}$	mode III critical length according to PM estimated from two notched specimen geometries
LM	line method
N_f	number of cycles to failure
PM	point method
R	load ratio
rms	root mean square
S	standard deviation
S_U	ultimate tensile strength
S_Y	yield strength
TCD	theory of critical distances
α, β	material parameters of a multiaxial fatigue criterion
$\bar{\alpha}$	notch opening angle
$\Delta\sigma_{fl}$	plain fatigue strength range
$\Delta\sigma_{N,fl}$	notch fatigue strength range
$\Delta\sigma_{fl}^*$	intrinsic plain fatigue strength range
ϕ	phase shift angle between axial and torsional load waveforms
λ	biaxiality
$\sigma_{N,a}$	nominal axial stress amplitude on the net cross-section
σ_w	high cycle fatigue strength predicted by $\sqrt{area}$ models
$\tau_{N,a}$	nominal torsional stress amplitude on the net cross-section calculated on the outer surface

Subscripts

1	sharp notch
2	blunt notch

1. Introduction

Ductile cast iron (DCI), also known as nodular cast iron or spheroidal graphite iron, finds increasing application in the production of moderately stressed components for the wind energy, handling and transport,

machine tool, presses and infrastructure industries [1]. The high castability conferred by its high carbon content allows the fabrication of parts with intricate geometries, such as gearboxes, crankshafts, and planet carriers [2]. The addition of Si- and Mg-based inoculants promote the precipitation of carbon in the form of spheroidal graphite particles, conferring superior ductility [3], [4] and, ultimately, higher fatigue strength compared to other grades of cast iron [5], [6]. Adequate fatigue properties are achieved only under a strict control of the microstructure, which mainly depends on the chemical composition and the solidification conditions [7]. Typical casting defects that adversely affect the mechanical properties of thick-walled castings, especially fatigue strength, are degenerate graphite [8] and microshrinkage porosity [9]. The formation of chunky degenerate graphite can be fought by adding small amounts of Sb [10] or Bi [11], while the appearance of pores and / or the overgrowth of graphite nodules can be shifted to less critical locations of the component by accelerating the solidification phase through localized heat removal. To this regard, Vaško et al. [5] showed that a microstructure with more but smaller graphite nodules has better mechanical properties and, in turn, higher fatigue strength.

Extensive research has been carried out so far to devise fatigue assessment methods able to take into account the role of defectiveness on the fatigue strength of DCI [9], [12]. Such defects may show even a large scatter in size, on the order of hundreds of microns, and an interesting correlation was found by Nasr et al. [12] between the S-N curves and the ranges of size of the observed defects. Endo and Yanase [13] noticed initiation from both shrinkage pores and in regions where no cavities were present, thus they considered as possible initiation sites not only shrinkage pores but also graphite nodules, and they evaluated the lower bound of the fatigue limit according to the well-known Murakami equation [14]. This relates Vickers hardness and the $\sqrt{area}$ parameter, to the power of 1/6, with the fatigue limit. Modifications to this model have recently been proposed to incorporate the effect of the load ratio [15]. Borsato et al. [16] replaced Vickers hardness with a combination of ultimate strength and yield strength to better capture the effect of nodular graphite morphology. The investigations reported so far were mainly carried out on plain samples, where the fatigue strength is dominated by the most critical defect in terms of sqrt(area). This scenario is however even more complicated in the case of notch fatigue [17], [18]. The non-homogeneous stress distribution introduced by the notch makes the defects differently critical against fatigue not only depending on their $\sqrt{area}$ but also on their location with respect to the notch stress peak. In a recent investigation [19], we found a significant difference in the defectiveness triggering the fatigue damage. In plain samples, a few and large shrinkage pores were found in the gage section through computed tomography (CT) analyses. The largest of them was responsible for the initiation of fatigue cracks. In notched samples, the likelihood that such a critical pore is in the process zone ahead of the notch tip is very low; therefore, the fatigue damage was promoted by the largest graphite nodule located therein. This evidence has important consequences when devising a notch fatigue assessment method for DCI. For example, when the Theory of Critical Distances (TCD) [20] is applied to predict the notch fatigue strength of DCI, a fatigue strength and a critical distance length that are actually representative of the local properties of the material that rule in the neighborhood of the tip of the notch must be used. In [19], we found that these fatigue properties are captured more effectively by an inverse search procedure based on the use of

two optimized notched geometries that differ in the radius of the root of the notch and therefore in the resulting stress concentration factor. A better agreement with the experimental data was obtained with respect to predictions made with critical distance estimations based on the plain fatigue strength and/or the crack growth threshold affected by fatigue and crack shielding mechanisms [21] not representative of those occurring at the notch tip. The necessity of adjusting the plain fatigue strength to the length scale of the fatigue damage that occurs in the notched components was also noted in [22], [23] where a probabilistic notch fatigue assessment was devised.

Since components made of DCI are typically exposed in service to complex time-varying loads, the present paper aims to extend the research described above to the multiaxial notch fatigue strength of DCI. To date, the multiaxial fatigue strength of this material class has been investigated in a few publications [24]–[26]. They permitted to highlight the peculiar fatigue characteristic of DCI resulting in preferential crack initiation on planes undergoing the largest normal stress amplitude, in contrast to conventional structural metals in which this mechanism is usually governed by the largest shear stress amplitude. Berto et al. [27] investigated the multiaxial fatigue strength of severely notched cast iron specimens and were able to rationalize the experimental results according to an average strain energy density approach [28] only by introducing two different sizes of the control volume under axial and torsional types of loading. A similar finding was found in a very recent publication [29] aimed at devising an inverse search approach of the TCD critical length under mode III type of loading. Fatigue experiments carried out on 42CrMo4 steel specimens tested under axial and torsional loading attested critical distance lengths that differ by a factor of about 9. Similar differences were found for 39NiCrMo3 steel [30] and PMMA [31]. Despite this experimental evidence, the applications of TCD to multiaxial fatigue reported in the literature [32] assume for the sake of simplicity the same value of mode I and mode III critical lengths. On the base of this literature survey, it is evident that still unexplored issues in the multiaxial notch fatigue assessment, especially of DCI, need to be addressed. For this reason, the present paper aims to investigate (i) which multiaxial fatigue criterion can be suitably combined with TCD to predict the notch fatigue strength of DCI; (ii) whether the critical distance length of DCI depends on the loading mode and how this dependency can be incorporated into a multiaxial fatigue criterion; (iii) how defectiveness affects the multiaxial fatigue properties of DCI. Accordingly, this paper is organized as follows. Section 2 describes the DCI investigated in this work and the procedures for its experimental characterization. Section 3 illustrates the results of the fatigue tests and fractographic analyses. In Section 4, the critical distance length of the material is deduced according to a procedure based on two notch variants. The mathematical formulation is available in [19] for the axial loading and described in Appendix A of the this paper for the torsional loading. The entire procedure can be found as an editable script file for the MATLAB® software in Appendix B. Section 5 analyzes the ability of some multiaxial fatigue criteria in combination of the TCD approach devised in Section 4 to predict the multiaxial plain and notch fatigue strength of DCI. Concluding remarks are given in Section 6.

2. Material and experimental procedures

The experimentation was carried out on an EN-GJS-600–3 pearlitic DCI. Details about the chemical composition, solidification conditions, and microstructure can be found in our recent publication [19]. The quasi-static mechanical properties are listed in Table 1.

The fatigue characterization was carried out using the axisymmetric specimen geometries illustrated in Figs. 1a-i. Specifically, the plain (smooth) specimen geometry shown in Figs. 1a and b was used to determine the material's baseline fatigue S-N curve under monoaxial and multiaxial loading, respectively. The V-notched specimen geometries reported in Fig. 1c-i are characterized by a notch depth that was optimized in [33] and [29] to maximize the intensity of the asymptotic stress field term under axial and torsional loading, respectively. In this way, it is possible to minimize the sensitivity of the inverse search of the critical distance to the experimental uncertainties. Specimens (c-e) and (f-h) have a V-notch opening angle of 60° and differ only in the notch tip radius and are referred to as "sharp" and "blunt" notches, respectively. Specimen (i) has a V-notch opening angle of 90° and will be used to collect independent fatigue results to validate the mean stress sensitivity of the devised fatigue assessment methods. Because of the fundamental role played by the notch root radius on the notch stress field, its actual value was verified by means of stereomicroscopic measurements and reported in Table 2 along with the corresponding theoretical stress concentration factor K_t. The measured notch root radii reported in Table 2 were used in the following TCD calculations.

Specimens (a), (c), (f) and (i), provided with threaded ends, were tested under axial fatigue loading according to the ASTM E466 standard in a laboratory environment using two Rumul (Switzerland) Testronic resonant testing machines, operating at a nominal frequency of 150 Hz under load control, one with 150 kN and the other with 50 kN load capacity. Specimens (a), (c) and (f) were tested under zero mean stress (load ratio R = − 1), while specimens (i) under load ratio R = 0.1.

The remaining specimens provided with flat cylindrical ends were fatigue tested in a laboratory environment using a Walter + Bai (Switzerland) LFV100-T1000-HH biaxial servo-hydraulic testing machine equipped with hydraulic grips and a biaxial load cell with axial and torsional load capacities of 100 kN and 1000 Nm, respectively. The load control imposed a sinusoidal waveform with a frequency comprised between 15 and 20 Hz, depending on the geometry of the specimen. Specifically, fully reversed (R = − 1) pure torsional loading was applied to a batch of samples (b), (d), and (g). Finally, batches of samples (b), (e), (h) were subjected to combined tension and torsion loading with load ratio R = − 1 and biaxiality ratio $\lambda = 1$. The latter expresses the ratio of the nominal torsion shear stress amplitude τ_a (calculated on the specimen outer surface) to the nominal axial stress amplitude σ_a. Two phase angles ϕ were explored, namely $\phi=0°$, in-phase loading, and $\phi=90°$, out-of-phase loading.

The medium-to-high-cycle fatigue life in the range between nearly 5×10^4 and 5×10^6 cycles was explored employing at least 12 plain or notched specimens, and runout tests were terminated at 5×10^6 cycles when no fracture took place. The axial fatigue curves corresponding to the probability of 50% failure were represented by the following asymptotic equation to smoothly capture the knee exhibited by the experimental SN data:

$$\sigma_a = k_1 + \frac{k_2}{N_f^{k_3}} \qquad (1a)$$

Torsional and combined axial and torsional fatigue tests did not show an appreciable change in the slope of the SN curve, which was then expressed by the well-known Basquin's equation:

$$\sigma_a = \frac{k_2}{N_f^{k_3}}; \quad \tau_a = \frac{k_2}{N_f^{k_3}} \qquad (1b)$$

The coefficients k_j (j=1,2,3) were determined by fitting the $\log(N_f)$ versus $\log(\sigma_a)$ or $\log(\tau_a)$ results. The scatter of the fatigue data was assessed by computing the estimated regression variance which was assumed to be uniform for the entire fatigue life range, and expressed by:

$$S^2 = \frac{\sum_{i=1}^{n}\left(\sigma_{a,i} - \hat{\sigma}_{a,i}\right)^2}{n - p}; \quad S^2 = \frac{\sum_{i=1}^{n}\left(\tau_{a,i} - \hat{\tau}_{a,i}\right)^2}{n - p} \qquad (2)$$

where $\sigma_{a,i}$ ($\tau_{a,i}$) is the i-th fatigue amplitude data point, $\hat{\sigma}_{a,i}$ ($\hat{\tau}_{a,i}$) is its estimator, n is the number of data elements, and p is the number of parameters in the regression ($p = 2$ or 3 in the present case).

Material characterization was complemented by fractographic analyzes carried out on fatigued samples using a JEOL JSM-IT300LV scanning electron microscope (SEM). Care was taken in identifying the microstructural feature triggering the fatigue damage. In addition, small coupons (6.5 mm diameter) were extracted from the same casting and analysed through metrological X-ray computed tomography (CT). In this way, it was possible to detect and measure internal voids as well as graphite nodules in terms of dimension (projected area and maximum Feret diameter), shape, and position. More details on the experimental procedures are given in [19].

3. Experimental results and discussion

The results of the fatigue tests carried out on all the specimen variants are compared in Fig. 2. Fitting curves corresponding to 50% (solid line), 10% and 90% (dashed lines enclosing a colored scatter band) failure probability, expressed by Eq. (1), are also plotted in Fig. 2. The best-fit parameters, the fatigue strength at 5×10^6 cycles, and the standard deviation S are listed in Table 3. Figures 2a-d report the results of fatigue experiments carried out on plain and notched specimens under pure axial, pure torsional, combined in-phase and combined out-of-phase axial and torsional loading, respectively.

Looking at Fig. 2a, it can be observed that the fatigue curves of the plain notched variants tested at R = − 1 approximately scale according to the notch stress concentration factor K_t. The application of a positive mean stress to the sharp notched samples (i) tested at R = 0.1 results in a considerable reduction in fatigue strength, which confirms the remarkable mean stress sensitivity of DCI [15], [27], [34]. The scenario depicted by the pure torsional tests shown in Fig. 2b is completely different: the blunt notched specimens exhibit the highest fatigue strength, while the smooth sample displays an intermediate behavior in the medium- and even the lowest fatigue strength in the high-cycle fatigue (HCF) regime. On the contrary, the application of the axial stress in the combined axial and torsional fatigue tests (Fig. 2c-d) restores the expected decreasing strength order: plain, blunt, and sharp-notched specimens, especially in the case of out-of-phase loading (Fig. 2d), on

which the effect of the axial stress is more evident. When comparing Figs. 2c and d, it can be noted that in-phase loading results in slightly lower fatigue strength, thus confirming the load phase effect already observed for DCI in [26].

SEM analyses were conducted to identify the dominant crack initiation mechanisms acting in the HCF regime in all the investigated experimental conditions. A meaningful example of the crack initiation site found in plain specimens is illustrated in Fig. 3a, c-d, g-h, and i, for axial, torsional, in-phase and out-of-phase combined loads, respectively. Importantly, in all the smooth samples investigated, the crack was found to start in the vicinity of a large near-surface solidification shrinkage pore, whose intricate geometry is indicated by red arrows. Completely different is the scenario depicted by the notched variants in Fig. 3b, e-f, j-k, and l for axial, torsional, in-phase and out-of-phase combined loads, respectively. In fact, the crack initiation site (marked by a red arrow) was found in the vicinity of a large graphite nodule or near the crater left by the fractured graphite nodule located in the neighborhood of the notch tip. Similar findings were found in [13] for DCI tested under rotating bending fatigue, which, similarly to notches, introduces a notable stress gradient towards the interior of the specimen, thus inhibiting crack initiation from most of the few pores located immediately below the outer surface or close to the notch tip.

SEM micrographs shown in Fig. 3 also give indications about the morphology of the fracture surface. Axial loading resulted in crack propagation orthogonal to the specimen axis in both plain (Fig. 3a) and notched specimens (Fig. 3b). Torsional loading promoted the early crack propagation on a plane inclined with respect to the specimen axis, especially in the plain sample (Fig. 3c). The notch forced the crack to remain on the notch bisector plane, resulting in a factory roof type of fracture morphology (Fig. 3e). However, the factory roof morphology is much less pronounced than that reported for more ductile metals, such as steel [35] or Ti alloys [36]. The combined in-phase and out-phase loading promoted crack propagation inclined with respect to the specimen axis in the plain sample (Figs. 3g and i) and growth of multiple cracks inclined with respect to the specimen axis in the notch sample (Figs. 3k and l). Out-of-phase loading produced flatter and smoother fracture surfaces. This has been attributed in [27] to abrasion and consequent debris creation produced by the interfering crack faces loaded under torsion when no axial loading is applied.

To shed light on the inclination of the fatigue crack initiated in fractured plain samples photographs were taken in the vicinity of the crack initiation site. They are reported in Fig.4a-d, for specimens tested under axial, pure torsion, combined in-phase and out-of-phase loads, respectively. Interestingly, the crack growth plane is approximately inclined orthogonally to the maximum principal stress axis under axial, torsion, and combined in-phase loading, i.e. when the direction of the principal stress axis is fixed over time (proportional loading). The direction of the principal stress axis is, in fact, inclined by an angle of 0°, 45° and 58°, respectively. Conversely, the out-of-phase load results in a higher inclination angle of the crack propagation plane (66°), thus indicating that the axial loading influences on a larger extent the crack propagation plane with respect to the torsion.

4. Inverse search of mode I and mode III critical distances

A robust notch fatigue assessment method needs to take into account the material's notch sensitivity factor [37]. TCD provides an effective tool for this purpose, as it can be easily combined with several multiaxial fatigue criteria [38]–[41]. The TCD postulates that a notched or cracked component is under fatigue critical conditions when a suitable stress component averaged over a domain of a certain critical size equals a stress value representative of the fatigue failure in a smooth part. For this reason, the critical length could be in principle indifferently deduced from two independent specimen geometries, of which at least one carries a stress raiser. However, this assumption might be inappropriate if the fatigue damage mechanism is controlled by a length-scale dependent defectiveness, as in the DCI under examination. As demonstrated by the fractographic analyzes portrayed in Fig. 3, the fatigue damage of plain samples is controlled by a few large defects (pores) dispersed in the large gage volume of the specimen, while that affecting notched samples is governed by much smaller graphite nodules located in the immediate vicinity of the notch tip. This scenario is well explained by the elaboration of CT analyses done in [19] on the defect distribution detected in the present material. Figure 5a illustrates the statistical distribution of pores and graphite nodules elaborated according to the statistics of the largest extreme value distribution (LEVD) using the Maximum Likelihood Method [14], [42]. Specifically, all pores detected in the scanned volume are included in this analysis, while only the graphite nodules comprised in a toroidal volume centered on the notch tip and having a radius equal to the critical distance determined in [19]. It can be noted that the maximum expected nodule size $\sqrt{area}_{\max}$ corresponding to a cumulative probability F of 99% is much smaller in the case of graphite nodules (156 μm) than in that of pores (1137 μm). In addition, nodules are found to have an approximate spheroidal shape, while pores exhibit a very intricate 3D geometry, as demonstrated by the CT reconstruction shown in Fig. 5b. We expect therefore that the plain fatigue strength is not representative of the intrinsic fatigue strength of the material in the immediate neighborhood of the notch tip. The interesting investigations done in [43] also highlighted the need to investigate the damage mechanisms of DCI on a microscopic scale. For this purpose, we proposed in [19] to deduce the critical distance L^* under axial loading from two notched specimen geometries, whose fatigue characteristics are representative of the fatigue damage occurring at the notch tip. In this paper, we extend this approach to the determination of intrinsic fatigue strength $\Delta\tau_{\mathrm{fl}}^*$ and critical distance length L_{T}^* under torsional loading. The mathematical formulation is explained in Appendix A.1 for both the line (LM) and point (PM) of the TCD and is based on the inverse search procedure proposed in [29] for mode III type of loading. Appendix A.2 describes the use of an editable MATLAB script, available with the online version of this paper, for a rapid implementation of the two proposed procedures.

The results of this double-notch inversion method according to the LM applied under axial and torsional loading are summarized in Table 4. The input fatigue properties were taken from the SN curves measured on sharp and blunt notch specimen geometries tested under axial (specimens (c) and (f)) and torsional (specimens (d) and (g)) loading. Figure 6 shows the results of Monte Carlo simulations carried out according to the procedure described in [44] to assess the effect of the stochasticity of the input fatigue properties on the statistical distribution of the intrinsic fatigue strength and the critical distance length. In summary, the input properties are assumed to obey a Gaussian distribution from which random variates are extracted to generate

individuals that are then organized in the histograms shown in Fig. 6a and b, for the critical length and the intrinsic fatigue strength, respectively. Looking at Fig. 6a, it can be noted that L^* and L_T^* exhibit a unimodal probability density function (PDF) with a longer right-side tail. The two statistical distributions are little overlapped (the mean values differ by a factor of 2.5), thus supporting the idea that DCI displays a distinct notch sensitivity under axial and torsional loading. The intrinsic fatigue strengths shown in Fig. 6b and listed in Table 4 exhibit a much more symmetric unimodal PDF. The two distributions are largely overlapping, thus confirming experimental evidences that the fatigue strength of DCI is dominated by the first principal stress, resulting in nearly equal axial and torsional fatigue limit [26]. Interestingly, as widely discussed in [19] and summarized in Table , the axial intrinsic fatigue strength $\Delta\sigma_{fl}^* / 2$ is in very good agreement with the HCF fatigue strength predicted by the following expression proposed by Borsato et al. [16]:

$$\sigma_W = \frac{F_{loc}\left(0.62 \cdot S_U + 0.32 \cdot S_Y\right)}{\left(\sqrt{area}_{max}\right)^{1/6}} \tag{3}$$

if the critical defect size $\sqrt{area}_{max}$ is taken equal to that of the largested expected graphite nodule indicated in Fig. 5a and the location factor F_{loc} is taken equal to 1.56 (internal defect). In this case, $\sigma_W = 269$ MPa is obtained. It is also interesting to observe that the ratio $\Delta\tau_{fl}^* / \Delta\sigma_{fl}^* = 0.90$ agrees very well with the values of 0.85 and 0.95 reported for DCI in [45] and [26], respectively. Similar findings have also been reported for an AISI 4140 steel weakened by hard nonmetallic inclusions [46].

To summarize, we can observe that the devised double-notch inversion method is able to predict fatigue strength values consistent with the defectiveness found in the vicinity of the notch tip and indicates a different material's notch sensitivity under axial and torsional loading. In particular, the longer mode III critical length L_T^* supports empirical evidences reported in the technical literature [30], [35] of a notch-strengthening effect under torsion due to the tendency of the crack to form a factory roof morphology. All these considerations will be used in the next section to identify suitable multiaxial fatigue criteria in combination with a TCD approach to notch sensitivitiy.

5. Multiaxial fatigue criteria

In this paper, we will focus our attention on critical plane (CP) based approaches, since strain energy- and stress invariants-based approaches cannot be applied to nonproportional (out-of-phase) loading. We will consider CP approaches according to Fatemi- Socie [47], Modified-Wöhler-Curve-Method (MWCM) [48] and Carpinteri et al. [49], since in [38], [40], [41], [50] they were successfully applied in combination with TCD. In view of the important role of the principal stress evidenced in Section 3, we will also explore a modification of the SWT normal stress CP criterion [51] proposed by Chu [52] and effectively used in [53] to assess the fatigue strength in the presence of multiaxial residual stresses.

The Fatemi-Socie criterion is based on the identification of the CP experiencing the maximum range of shear strain γ_a. Furthermore, it incorporates the mean stress using the maximum value of the normal stress $\sigma_{n,max}$, acting on the plane of the maximum shear strain range:

$$\gamma_a \left(1 + \alpha_{FS} \frac{\sigma_{n,\max}}{S_Y} \right) = \beta_{FS} \tag{4}$$

where S_Y is the material's yield stress.

The MWCM is a CP-based criterion, which may be written as:

$$\tau_a + \alpha_{MWCM} \frac{\sigma_{n,\max}}{\tau_a} = \beta_{MWCM} \tag{5a}$$

where the amplitude of the shear stress a and the maximum normal stress $\sigma_{n,\max}$ are calculated on the CP that experiences the largest amplitude of the shear stress. This fatigue criterion must satisfy the condition:

$$\frac{\sigma_{n,\max}}{\tau_a} \le \frac{\beta_{MWCM}}{2\alpha_{MWCM}} \tag{5b}$$

since, beyond this upper limit, material failure is expected to be no longer influenced by the amplitude of shear stress [48].

Carpinteri et al. [39] observed that the CP orientation depends on the ductility of the material and assumed it to be a function of the fully reversed axial and torsional fatigue strength σ_{AF}, τ_{AF}. Accordingly, the normal to the CP is assumed to be inclined by the angle δ with respect to the averaged direction of maximum principal stress expressed as:

$$\delta = \frac{3\pi}{8} \left[1 - \left(\frac{\tau_{AF}}{\sigma_{AF}} \right)^2 \right] \tag{6a}$$

The fatigue criterion is a quadratic combination of the shear stress amplitude τ_a and the normal equivalent stress $\sigma_{n,eq}$ acting on the CP:

$$\sqrt{\sigma^2_{n,eq} + \left(\frac{\sigma_{AF}}{\tau_{AF}} \right)^2 \tau_a^2} = \sigma_{AF} \tag{6b}$$

Where $\sigma_{n,eq}$ is a linear (Goodman) combination of the amplitude $\sigma_{n,a}$ and the mean value $\sigma_{n,m}$ of the normal stress component [49]:

$$\sigma_{n,eq} = \sigma_{n,a} + \sigma_{AF} \left(\frac{\sigma_{n,m}}{S_U} \right) \tag{6c}$$

where S_U is the ultimate tensile strength of the material.

The modified SWT criterion is expressed by:

$$\left(2\alpha_{mSWT} \Delta\varepsilon \langle \sigma_{\max} \rangle + \frac{1 - \alpha_{mSWT}}{2} \Delta\tau\Delta\gamma \right)_{\max,\theta} = \beta_{mSWT} \tag{7}$$

where and are the normal stress and shear stress, respectively, in a material plane. ε and γ are the normal strain and the shear strain, respectively. The symbol Δ denotes range in a loading cycle. The symbol $\langle \ \rangle$ represents

the MacCauley bracket ($\langle x \rangle = (x + |x|)/2$). The CP is defined as the material plane that experiences the maximum fatigue parameter β_{mSWT}.

The two-parameter fatigue criteria described above will be used in combination with the LM of TCD to predict the experimental data collected in this work. LM was selected instead of PM because it proved in [50] to yield more accurate predictions when used in conjunction with a multiaxial fatigue criterion. As schematically illustrated in Fig. 7a, the axial normal σ_i ($i=r$, θ, z) and torsional shear stresses $\tau_{z\theta}$ are averaged along the notch bisector over the material's critical distances according to two distinct approaches, termed "4p" and "3p". In "4p", the two critical distances L and L_T are allowed to take different values, while in "3p" a unique critical distance is imposed for both mode I and III types of loading. In the former case, the resulting multiaxial+TCD fatigue criterion depends on four materials parameters (whence the notation "4p"), whereas in the latter one on three parameters ("3p") only.

A careful reader might object that the adopted formulation of TCD in combination with a CP-based fatigue criterion is in contrast with many similar attempts [40], [41] proposed in the literature, wherein the stresses are averaged along a path lying on the CP. However, we deem our approach reasonable, mainly for the following motivations: (i) the proposed approach is of easier implementation, as it does not require to average the stresses along a CP of unknown inclination, therefore an iterative procedure is not necessary; (ii) empirical evidence, also shown in Section 3 and other relevant literature [50], [54], attest to the propensity of fatigue cracks to extend along the notch symmetry plane; (iii) a systematic analysis [55] comparing the fatigue calculations performed averaging the stress components along either the notch bisector or the CP did not show any significant difference in prediction accuracy.

The four or three material-dependent parameters of the fatigue criteria described above are calibrated from four or three independent fatigue data. More specifically, the axial and torsional fully-reversed fatigue strength of sharp- and blunt-notched specimens are used in the calibration of the "4p" approach, while the parameters of the "3p" approach are calibrated on the basis of the axial fatigue strength of both notched geometries as well as of the torsional fatigue strength of the sharp-notched variant only. The values of the parameters calibrated in the HCF regime ($N_f=5\times10^6$) are listed in Table 5. The superscript "*" denotes the fact that the parameters were inferred from notched geometries, therefore they are representative of fatigue properties reflecting the defectiveness ruling the notch tip region. Interestingly, the critical distance values according to the 4p method are identical to less than a few microns to those listed in Table 4 and assessed using the double notch inversion method applied separately to the axial and torsional loading. Therefore, this latter method turns out to be very useful also for the calibration of multiaxial fatigue criteria. Furthermore, the material parameters σ_{AF}^*, τ_{AF}^* of Carpinteri et al. criterion are nearly identical to the intrinsic fatigue strengths listed in Table 4. Finally, it can be observed that the unique critical distance assumed by the "3p" method is close to the mode I critical distance assessed according to the corresponding "4p" method. Lastly, the conditions set according to the "3p" method for the MWCM resulted in an equation system with no real roots. Therefore, in the following, no predictions will be made according to this approach.

Table 6 compares the fatigue criteria in terms of prediction accuracy of the HCF strength of independent load conditions applied to notched specimens not used for the criterion calibration. Looking at the "4p" methods, it can be observed that Carpinteri et al. and modified SWT criteria are the only ones able to keep the maximum absolute error and the rms error below 15% and 10%, respectively. This is not surprising given the important role played in DCI by the maximum normal tensile stress, whose influence is better captured by the last-mentioned criteria. In particular, the nearly equal values of the materials parameters σ_{AF}^{*}, τ_{AF}^{*} of Carpinteri et al. criterion make the angle δ nearly equal to zero, thus making preponderant the contribution of the normal equivalent stress $\sigma_{n,eq}$ acting on the CP. The shear-based criteria of Fatemi-Socie and especially of MWCM are instead affected by larger errors. When we focus on "3p" methods, we can observe that assuming the same notch sensitivity factor under tension and torsion leads to a certain error in the estimation of the blunt-notched variant under pure torsion. More importantly, the calibration of the Carpinteri et al. criterion under this assumption leads to some inaccuracies in the estimation of the materials parameters σ_{AF}^{*}, τ_{AF}^{*} and, ultimately, in fatigue estimations affected by largest maximum absolute and rms erros. In summary, we can conclude that a correct assessment of the multiaxial notch fatigue strength of DCI requires a normal stress-based fatigue criterion that incorporates the different notch sensitivity of the material under mode I and III loading.

For these reasons, in the next we further develop only the Carpinteri et al. criterion in the "4p" formulation, as it proved to ensure the lowest maximum absolute error and rms error among the explored approaches. A first improvement of this approach is its extension to the prediction of the fatigue strength in the presence of defectiveness different from that present in coupons used for its calibration, for instance, the microshrinkage porosity found in plain specimens. To this regard, it is interesting to check if Eq. (3) can correctly predict the axial plain fatigue strength. The estimations listed in Table 7 were obtained considering the maximum expected pore size corresponding to a cumulative probability F of 99% (see Fig. 5a). The pore size is expressed in terms of both the square root of the area projected on the plane normal to the loading axis and the maximum Feret diameter d_{F}. It can be noted that the prediction made considering this latter definition of the pore size is in very good agreement with the experimental data. When analyzing the fatigue strength of cast Al-alloys, Wang et al. [56] and later Nicoletto et al. [57] came to the same conclusion, viz. the effect of the intricate geometry of microshrinkage pores (see Fig. 5b) is better captured by d_{F}. For this reason, we propose to tune the parameters σ_{AF}, τ_{AF} of plain samples weakened by pores of characteristic size d_{F} by rescaling the intrisic fatigue characteristics σ_{AF}^{*}, τ_{AF}^{*} according to the 1/6 power law dependency upon the defect size expressed by Eq. (3):

$$\sigma_{AF} = \sigma_{AF}^{*} \left(\frac{\left. \sqrt{area}_{max} \right|_{nodule}}{\left. d_{F} \right|_{pore}} \right)^{1/6} \quad ; \quad \tau_{AF} = \tau_{AF}^{*} \left(\frac{\left. \sqrt{area}_{max} \right|_{nodule}}{\left. d_{F} \right|_{pore}} \right)^{1/6} \tag{8}$$

A careful reader might object that the pore size should also be in terms of Feret diameter. This leads however to negligible differences given the nearly spherical shape exhibited by graphite nodules.

Table 8 lists the values of σ_{AF}, τ_{AF} and the prediction of the plain fatigue strength in the explored loading conditions. It can be noted that the maximum absolute error and the rms error are on the same order of magnitude of those listed in Table 7 for the notch fatigue predictions, thus confirming the possibility of extending the calibration of the proposed approach to fatigue scenario affected by defectiveness different from those present in notched geometries used for the parameter calibration.

To conclude, the present fatigue calculation method is extended to the medium cycle fatigue regime. Therefore, the four criterion parameters are calibrated from sharp- and blunt- notch axial and torsional fatigue data taken at different fatigue lives N_f. Their dependency on N_f is shown in Fig. 8a. As expected, the intrinsic plain fatigue strengths σ_{AF}^*, τ_{AF}^* decrease with increasing number of cycles to failure, whereas the critical distances L^* and L_T^* are fairly independent of N_f. Figure 8b,c,d plots the SN curves calculated for the sharp-, blunt-notched, and smooth geometries, respectively. In the last case, the fatigue calculations are done using σ_{AF}, τ_{AF} deduced from σ_{AF}^*, τ_{AF}^* according to Eq. (8). The predicted SN curves agree well with the trend of the experimental data, especially for long fatigue lives ($N_f \geq 5 \times 10^6$). In any case, the predicted data fall in an error band comprised between ±15%, which is reasonable given the large dispersion in the fatigue properties of the investigated material.

6. Conclusions

This paper explored the multiaxial fatigue strength of a ductile cast iron (DCI) EN-GJS-600–3 fabricated under conditions representative of heavy-section castings. Defects were characterized through fractographic and CT scan analyses. The fatigue data were used to calibrate a multiaxial fatigue criterion in combination with a TCD method to account for the material notch sensitivity. The following conclusions can be drawn:

1. Significant differences in the defectiveness that triggers fatigue damage were found in smooth and notched samples. In the former, the largest shrinkage pore is responsible for the initiation of fatigue crack. Its effect on fatigue strength is better captured by the maximum Feret diameter with respect to the projected area. In the latter, the fatigue damage is promoted by the largest, nearly spheroidal, graphite nodule located in the vicinity of the notch tip.

2. TCD critical lengths were deduced from notched specimen geometries with notches of different severity. In this way, it is also possible to infer the intrinsic fatigue strength of the material in the vicinity of the notch tip. The mode III critical distance L_T^* was found to be 3 times larger than that in mode I L^*, thus indicating a different material's notch sensitivity under torsion and axial loading.

3. The multiaxial fatigue behaviour of DCI was found to be predominantly controlled by the maximum principle stress. For this reason, normal stress-based criteria such as modified SWT and the Carpinteri et al. criteria were found to yield the most accurate fatigue predictions. This last criterion works best if it is combined with a TCD method considering different TCD critical lengths under mode I and III type of loading.

4. The devised multiaxial fatigue criterion can be extendend to multiaxial fatigue scenarios affected by defectiveness different from that present in the notched geometries used for its calibration through simple scaling of the material parameters according to the 1/6 power law dependency upon the defect size.

Appendix

A.1 Numerical example applied to the experimental data

In this appendix, the procedure for the determination of the torsional critical distance and the corresponding torsional fatigue limit is described. The procedure already presented in [19] is exploited by combining the fatigue strengths of two notches, namely a sharp and a blunt notch. The reported example refers to the experimental data reported above in Section 3. The geometry parameters are in Eq. A.1:

$$\bar{\alpha} = 60°$$
$$D_1 = 18.6\,\text{mm}, R_1 = 0.23\,\text{mm}$$
$$D_2 = 18.6\,\text{mm}, R_2 = 1.0\,\text{mm}$$

(A.1)

The size ratio with these two specimens is unity, $\Lambda = D_1 / D_2 = 1$, nevertheless this procedure can be used with different outer diameters of the two specimens, or even more generalized with different notch opening angles $\bar{\alpha}$, either 60° or 90°. The specimen 2 is the blunter, and hence the (nominal) fatigue limit is higher, Eq. A.2:

$$\Delta\tau_{\text{N,fl},1} = 344 \text{ MPa}$$
$$\Delta\tau_{\text{N,fl},2} = 383 \text{ MPa}$$

(A.2)

With these two torsional fatigue strengths as input, the ratio between the fatigue stress concentration factors can be obtained, even without the inherent (or plain specimen) fatigue limit which is an output of the procedure:

$$K_{\text{rT}} = \frac{K_{\text{fT},1}}{K_{\text{fT},2}} = \frac{\Delta\tau_{\text{fl}}^*}{\Delta\tau_{\text{N,fl},1}} \bigg/ \frac{\Delta\tau_{\text{fl}}^*}{\Delta\tau_{\text{N,fl},2}} = \frac{\Delta\tau_{\text{N,fl},2}}{\Delta\tau_{\text{N,fl},1}} = 1.114$$

(A.3)

From the geometry parameters in Eq. A.1, the torsional notch stress concertation factors can be initially evaluated, Eq. A.4:

$$K_{\text{tT},1} = 2.691$$
$$K_{\text{tT},2} = 1.675$$

(A.4)

The procedure optimal range of the torsional fatigue critical distance can be deduced from the formulation reported in [19], for both the two specimens, specimen 1: 0.0168 mm − 0.8110 mm, and specimen 2: 0.0543 mm − 1.2606 mm. The intersection of these two ranges is $L_{\text{T}}^* : 0.0543 \text{ mm} - 0.8110 \text{ mm}$. This critical distance range can be divided into many samples, such as 10^3, and for each value, the fatigue stress concertation

factors of the two samples can be deduced, and then the ratio can be easily calculated. In this way, the fatigue factor ratio curves can be obtained according to the Line and Point Methods, Fig. A.1.

Using a simple numerical interpolation tool, the critical distance of interception between the experimental K_{rT} value and the two curves is obtained. The resulting torsional critical distance L_T^* and the corresponding K_f values are listed below, in Eqs. A.5 and A.6, for the Line and the Point Methods, respectively:

$$L_T^* = 0.3325 \text{ mm}$$
$$K_{fT,1} = 1.405$$
$$K_{fT,2} = 1.262$$
(A.5)

$$L_T^{*\prime} = 0.4175 \text{ mm}$$
$$K_{fT,1} = 1.513$$
$$K_{fT,2} = 1.359$$
(A.6)

Since fatigue stress concentration factors are available now, the inherently fatigue limit can be easily deduced from the experimental strengths of the two notches. For each method, the fatigue limit is a unique result either obtained with specimen 1 or specimen 2, while, however, a small difference remains by comparing Line and Point methods, Eq. A.7:

$$\Delta \tau_{fl}^*(\text{LM}) = 483 \text{ MPa}$$
$$\Delta \tau_{fl}^*(\text{PM}) = 520 \text{ MPa}$$
(A.7)

A.2 Supplementary material

In the online version of the paper a MATLAB script file is available for quicky performing the calculation steps described in Appendix A.

References

[1]   C. Bleicher, H. Kaufmann, and T. Melz, "Assessment of service loads and material influence on the lifetime of thick-walled nodular cast iron components," *Int. J. Fatigue*, vol. 147, p. 106171, Jun. 2021, doi: 10.1016/j.ijfatigue.2021.106171.

[2]   T. Borsato, P. Ferro, A. Fabrizi, F. Berto, and C. Carollo, "Long solidification time effect on solution strengthened ferritic ductile iron fatigue properties," *Int. J. Fatigue*, vol. 145, p. 106137, Apr. 2021, doi: 10.1016/j.ijfatigue.2020.106137.

[3]   A. Ghahremaninezhad and K. Ravi-Chandar, "Deformation and failure in nodular cast iron," *Acta Mater.*, vol. 60, no. 5, pp. 2359–2368, Mar. 2012, doi: 10.1016/j.actamat.2011.12.037.

[4]   N. Bonora and A. Ruggiero, "Micromechanical modeling of ductile cast iron incorporating damage. Part I: Ferritic ductile cast iron," *Int. J. Solids Struct.*, vol. 42, no. 5–6, pp. 1401–1424, Mar. 2005, doi: 10.1016/j.ijsolstr.2004.07.025.

[5]   A. Vaško, L. Hurtalová, M. Uhríčik, and E. Tillová, "Fatigue of nodular cast iron at high frequency loading," *Materwiss. Werksttech.*, vol. 47, no. 5–6, pp. 436–443, Jun. 2016, doi:

10.1002/mawe.201600519.

[6]   H. Yaacoub Agha, A.-S. Beranger, R. Billardon, and F. Hild, "HIGH-CYCLE FATIGUE
        BEHAVIOUR OF SPHEROIDAL GRAPHITE CAST IRON," *Fract. Eng. Mater. Struct.*, vol. 21,
        no. 3, pp. 287–296, Mar. 1998, doi: 10.1046/j.1460-2695.1998.00293.x.

[7]   T. Borsato, P. Ferro, F. Berto, and C. Carollo, "Mechanical and fatigue properties of pearlitic ductile
        iron castings characterized by long solidification times," *Eng. Fail. Anal.*, vol. 79, pp. 902–912, Sep.
        2017, doi: 10.1016/j.engfailanal.2017.06.007.

[8]   P. Ferro, P. Lazzarin, and F. Berto, "Fatigue properties of ductile cast iron containing chunky
        graphite," *Mater. Sci. Eng. A*, vol. 554, pp. 122–128, Sep. 2012, doi: 10.1016/j.msea.2012.06.024.

[9]   Y. Nadot, "Influence of casting defects on the fatigue limit of nodular cast iron," *Int. J. Fatigue*, vol.
        26, no. 3, pp. 311–319, Mar. 2004, doi: 10.1016/S0142-1123(03)00141-5.

[10]   M. Benedetti, V. Fontanari, and D. Lusuardi, "Effect of graphite morphology on the fatigue and
        fracture resistance of ferritic ductile cast iron," *Eng. Fract. Mech.*, vol. 206, pp. 427–441, Feb. 2019,
        doi: 10.1016/j.engfracmech.2018.12.019.

[11]   T. Borsato, P. Ferro, F. Berto, and C. Carollo, "Fatigue strength improvement of heavy-section
        pearlitic ductile iron castings by in-mould inoculation treatment," *Int. J. Fatigue*, vol. 102, pp. 221–
        227, Sep. 2017, doi: 10.1016/j.ijfatigue.2017.02.012.

[12]   A. NASR, C. BOURAOUI, R. FATHALLAH, and Y. NADOT, "Probabilistic high cycle fatigue
        behaviour of nodular cast iron containing casting defects," *Fatigue Fract. Eng. Mater. Struct.*, vol.
        32, no. 4, pp. 292–309, Apr. 2009, doi: 10.1111/j.1460-2695.2009.01330.x.

[13]   M. Endo and K. Yanase, "Effects of small defects, matrix structures and loading conditions on the
        fatigue strength of ductile cast irons," *Theor. Appl. Fract. Mech.*, vol. 69, pp. 34–43, Feb. 2014, doi:
        10.1016/j.tafmec.2013.12.005.

[14]   Y. Murakami, *Metal fatigue: effects of small defects and nonmetallic inclusions.* Oxford: Elsevier,
        2002.

[15]   T. Deguchi, H. J. Kim, T. Ikeda, and K. Yanase, "Influence of mean stress on fatigue strength of
        ferritic-pearlite ductile cast iron with small defects," *J. Phys. Conf. Ser.*, vol. 843, p. 012049, May
        2017, doi: 10.1088/1742-6596/843/1/012049.

[16]   T. Borsato, P. Ferro, and F. Berto, "Novel method for the fatigue strength assessment of heavy
        sections made by ductile cast iron in presence of solidification defects," *Fatigue Fract. Eng. Mater.
        Struct.*, vol. 41, no. 8, pp. 1746–1757, Aug. 2018, doi: 10.1111/ffe.12815.

[17]   P. Livieri, E. Maggiolini, and R. Tovo, "On the notch sensitivity of cast iron under multi-axial fatigue
        loading," *Frat. ed Integrità Strutt.*, vol. 8, no. 30, pp. 558–568, Sep. 2014, doi: 10.3221/IGF-
        ESIS.30.67.

[18]   D. Taylor, M. Hughes, and D. Allen, "Notch fatigue behaviour in cast irons explained using a fracture
        mechanics approach," *Int. J. Fatigue*, vol. 18, no. 7, pp. 439–445, Oct. 1996, doi: 10.1016/0142-
        1123(96)00018-7.

[19] M. Benedetti, C. Santus, V. Fontanari, D. Lusuardi, F. Zanini, and S. Carmignato, "Plain and notch fatigue strength of thick-walled ductile cast iron EN-GJS-600-3: A double-notch critical distance approach to defect sensitivity," *Int. J. Fatigue*, vol. 152, p. 106414, Nov. 2021, doi: 10.1016/j.ijfatigue.2021.106414.

[20] D. Taylor, *The Theory of Critical Distances. A New Perspective in Fracture Mechanics*, 1st ed. Elsevier Science, 2007.

[21] M. Benedetti, J. Heidemann, J. O. Peters, and G. Lütjering, "Influence of sharp microstructural gradients on the fatigue crack growth resistance of α + β and near-α titanium alloys," *Fatigue Fract. Eng. Mater. Struct.*, vol. 28, no. 10, pp. 909–922, Oct. 2005, doi: 10.1111/j.1460-2695.2005.00932.x.

[22] D. Liao, S.-P. Zhu, B. Keshtegar, G. Qian, and Q. Wang, "Probabilistic framework for fatigue life assessment of notched components under size effects," *Int. J. Mech. Sci.*, vol. 181, p. 105685, Sep. 2020, doi: 10.1016/j.ijmecsci.2020.105685.

[23] J.-C. He, S.-P. Zhu, D. Liao, X.-P. Niu, J.-W. Gao, and H.-Z. Huang, "Combined TCD and HSV approach for probabilistic assessment of notch fatigue considering size effect," *Eng. Fail. Anal.*, vol. 120, p. 105093, Feb. 2021, doi: 10.1016/j.engfailanal.2020.105093.

[24] Marquis and Socie, "Long-life torsion fatigue with normal mean stresses," *Fatigue Fract. Eng. Mater. Struct. Fract. Eng. Mater. Struct.*, vol. 23, no. 4, pp. 293–300, Apr. 2000, doi: 10.1046/j.1460-2695.2000.00291.x.

[25] G. B. Marquis and P. Karjalainen-Roikonen, "Long-life multiaxial fatigue of a nodular graphite cast iron," 2003, pp. 105–122.

[26] R. Tovo, P. Lazzarin, F. Berto, M. Cova, and E. Maggiolini, "Experimental investigation of the multiaxial fatigue strength of ductile cast iron," *Theor. Appl. Fract. Mech.*, vol. 73, pp. 60–67, Oct. 2014, doi: 10.1016/j.tafmec.2014.07.003.

[27] F. Berto, P. Lazzarin, and R. Tovo, "Multiaxial fatigue strength of severely notched cast iron specimens," *Int. J. Fatigue*, vol. 67, pp. 15–27, Oct. 2014, doi: 10.1016/j.ijfatigue.2014.01.013.

[28] D. Liao, S. Zhu, J. A. F. O. Correia, A. M. P. De Jesus, and F. Berto, "Recent advances on notch effects in metal fatigue: A review," *Fatigue Fract. Eng. Mater. Struct.*, vol. 43, no. 4, pp. 637–659, Apr. 2020, doi: 10.1111/ffe.13195.

[29] C. Santus, F. Berto, M. Pedranz, and M. Benedetti, "Mode III critical distance determination with optimized V-notched specimen under torsional fatigue and size effects on the inverse search probability distribution," *Int. J. Fatigue*, vol. 151, p. 106351, Oct. 2021, doi: 10.1016/j.ijfatigue.2021.106351.

[30] F. BERTO, P. LAZZARIN, and J. R. YATES, "Multiaxial fatigue of V-notched steel specimens: a non-conventional application of the local energy method," *Fatigue Fract. Eng. Mater. Struct.*, vol. 34, no. 11, pp. 921–943, Nov. 2011, doi: 10.1111/j.1460-2695.2011.01585.x.

[31] L. Susmel and D. Taylor, "The theory of critical distances to predict static strength of notched brittle components subjected to mixed-mode loading," *Eng. Fract. Mech.*, vol. 75, no. 3–4, pp. 534–550,

Feb. 2008, doi: 10.1016/j.engfracmech.2007.03.035.

[32] L. Susmel and D. Taylor, "The Theory of Critical Distances to estimate finite lifetime of notched components subjected to constant and variable amplitude torsional loading," *Eng. Fract. Mech.*, vol. 98, pp. 64–79, Jan. 2013, doi: 10.1016/j.engfracmech.2012.12.007.

[33] C. Santus, D. Taylor, and M. Benedetti, "Determination of the fatigue critical distance according to the Line and the Point Methods with rounded V-notched specimen," *Int. J. Fatigue*, vol. 106, pp. 208–218, Jan. 2018, doi: 10.1016/j.ijfatigue.2017.10.002.

[34] N. Shinohara, N. Hattori, and M. T. I. Khan, "Effect of Mean Stress on Fatigue Strength of Spheroidal Graphite Cast Iron," *Mater. Sci. Forum*, vol. 750, pp. 192–195, Mar. 2013, doi: 10.4028/www.scientific.net/MSF.750.192.

[35] K. Tanaka, "Crack initiation and propagation in torsional fatigue of circumferentially notched steel bars," *Int. J. Fatigue*, vol. 58, pp. 114–125, Jan. 2014, doi: 10.1016/j.ijfatigue.2013.01.002.

[36] F. Berto, A. Campagnolo, and P. Lazzarin, "Fatigue strength of severely notched specimens made of Ti-6Al-4V under multiaxial loading," *Fatigue Fract. Eng. Mater. Struct.*, vol. 38, no. 5, pp. 503–517, May 2015, doi: 10.1111/ffe.12272.

[37] R. Budynas and J. Nisbett, *Shigley's mechanical engineering design*, 10th ed. McGraw-Hill Education, 2014.

[38] L. SUSMEL and D. TAYLOR, "The Modified Wöhler Curve Method applied along with the Theory of Critical Distances to estimate finite life of notched components subjected to complex multiaxial loading paths," *Fatigue Fract. Eng. Mater. Struct.*, vol. 31, no. 12, pp. 1047–1064, Dec. 2008, doi: 10.1111/j.1460-2695.2008.01296.x.

[39] A. Carpinteri, A. Spagnoli, S. Vantadori, and D. Viappiani, "A multiaxial criterion for notch high-cycle fatigue using a critical-point method," *Eng. Fract. Mech.*, vol. 75, no. 7, pp. 1864–1874, May 2008, doi: 10.1016/j.engfracmech.2006.11.002.

[40] N. Gates and A. Fatemi, "Notch deformation and stress gradient effects in multiaxial fatigue," *Theor. Appl. Fract. Mech.*, vol. 84, pp. 3–25, Aug. 2016, doi: 10.1016/j.tafmec.2016.02.005.

[41] C. Ronchei and S. Vantadori, "Notch fatigue life estimation of Ti-6Al-4V," *Eng. Fail. Anal.*, vol. 120, p. 105098, Feb. 2021, doi: 10.1016/j.engfailanal.2020.105098.

[42] S. Beretta and Y. Murakami, "Statistical analysis of defects for fatigue strength prediction and quality control of materials," *Fatigue Fract. Eng. Mater. Struct.*, vol. 21, no. 9, pp. 1049–1065, Sep. 1998, doi: 10.1046/j.1460-2695.1998.00104.x.

[43] M. Cavallini, O. Di Bartolomeo, and F. Iacoviello, "Fatigue crack propagation damaging micromechanisms in ductile cast irons," *Eng. Fract. Mech.*, vol. 75, no. 3–4, pp. 694–704, Feb. 2008, doi: 10.1016/j.engfracmech.2007.02.002.

[44] M. Benedetti and C. Santus, "Statistical properties of threshold and notch derived estimations of the critical distance according to the line method of the theory of critical distances," *Int. J. Fatigue*, vol. 137, p. 105656, Aug. 2020, doi: 10.1016/j.ijfatigue.2020.105656.

[45] M. Endo, "Effects of small defects on the fatigue strength of steel and ductile iron under combined axial/torsional loading," in *Small Fatigue Cracks*, Elsevier, 1999, pp. 375–387.

[46] P. V. S. Machado, L. C. Araújo, M. V. Soares, L. Reis, and J. A. Araújo, "Multiaxial fatigue assessment of steels with non-metallic inclusions by means of adapted critical plane criteria," *Theor. Appl. Fract. Mech.*, vol. 108, p. 102585, Aug. 2020, doi: 10.1016/j.tafmec.2020.102585.

[47] A. Fatemi and D. F. Socie, "A CRITICAL PLANE APPROACH TO MULTIAXIAL FATIGUE DAMAGE INCLUDING OUT-OF-PHASE LOADING," *Fatigue Fract. Eng. Mater. Struct.*, vol. 11, no. 3, pp. 149–165, Mar. 1988, doi: 10.1111/j.1460-2695.1988.tb01169.x.

[48] L. Susmel and P. Lazzarin, "A bi-parametric Wöhler curve for high cycle multiaxial fatigue assessment," *Fatigue Fract. Eng. Mater. Struct.*, vol. 25, no. 1, pp. 63–78, Jan. 2002, doi: 10.1046/j.1460-2695.2002.00462.x.

[49] A. Carpinteri, A. Spagnoli, and S. Vantadori, "Multiaxial fatigue assessment using a simplified critical plane-based criterion," *Int. J. Fatigue*, vol. 33, no. 8, pp. 969–976, Aug. 2011, doi: 10.1016/j.ijfatigue.2011.01.004.

[50] M. Benedetti and C. Santus, "Mean stress and plasticity effect prediction on notch fatigue and crack growth threshold, combining the theory of critical distances and multiaxial fatigue criteria," *Fatigue Fract. Eng. Mater. Struct.*, vol. 42, no. 6, pp. 1228–1246, Jun. 2019, doi: 10.1111/ffe.12910.

[51] K. N. Smith, P. Watson, and T. H. Topper, "A stress–strain parameter for the fatigue of metals," *J. Mater.*, vol. 5, no. 4, pp. 767–778, 1970.

[52] C.-C. Chu, "Fatigue Damage Calculation Using the Critical Plane Approach," *J. Eng. Mater. Technol.*, vol. 117, no. 1, pp. 41–49, Jan. 1995, doi: 10.1115/1.2804370.

[53] M. Benedetti, V. Fontanari, M. Bandini, and D. Taylor, "Multiaxial fatigue resistance of shot peened high-strength aluminum alloys," *Int. J. Fatigue*, vol. 61, pp. 271–282, Apr. 2014, doi: 10.1016/j.ijfatigue.2013.10.020.

[54] L. Susmel and D. Taylor, "Non-propagating cracks and high-cycle fatigue failures in sharply notched specimens under in-phase Mode I and II loading," *Eng. Fail. Anal.*, vol. 14, no. 5, pp. 861–876, Jul. 2007, doi: 10.1016/j.engfailanal.2006.11.038.

[55] D. Liao, S.-P. Zhu, and G. Qian, "Multiaxial fatigue analysis of notched components using combined critical plane and critical distance approach," *Int. J. Mech. Sci.*, vol. 160, pp. 38–50, Sep. 2019, doi: 10.1016/j.ijmecsci.2019.06.027.

[56] Q. G. Wang and P. E. Jones, "Prediction of Fatigue Performance in Aluminum Shape Castings Containing Defects," *Metall. Mater. Trans. B*, vol. 38, no. 4, pp. 615–621, Sep. 2007, doi: 10.1007/s11663-007-9051-4.

[57] G. Nicoletto, R. Konečná, and S. Fintova, "Characterization of microshrinkage casting defects of Al–Si alloys by X-ray computed tomography and metallography," *Int. J. Fatigue*, vol. 41, pp. 39–46, Aug. 2012, doi: 10.1016/j.ijfatigue.2012.01.006.
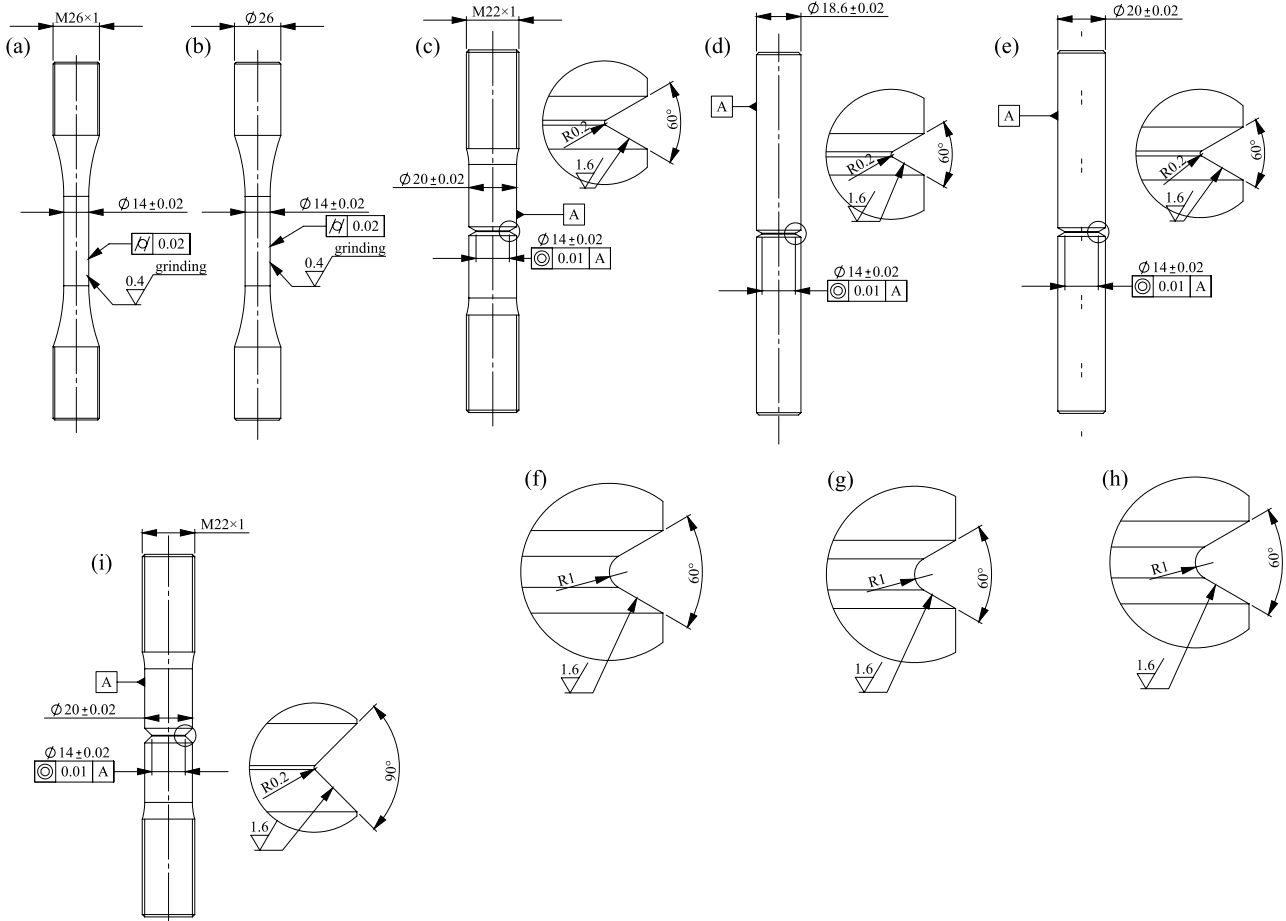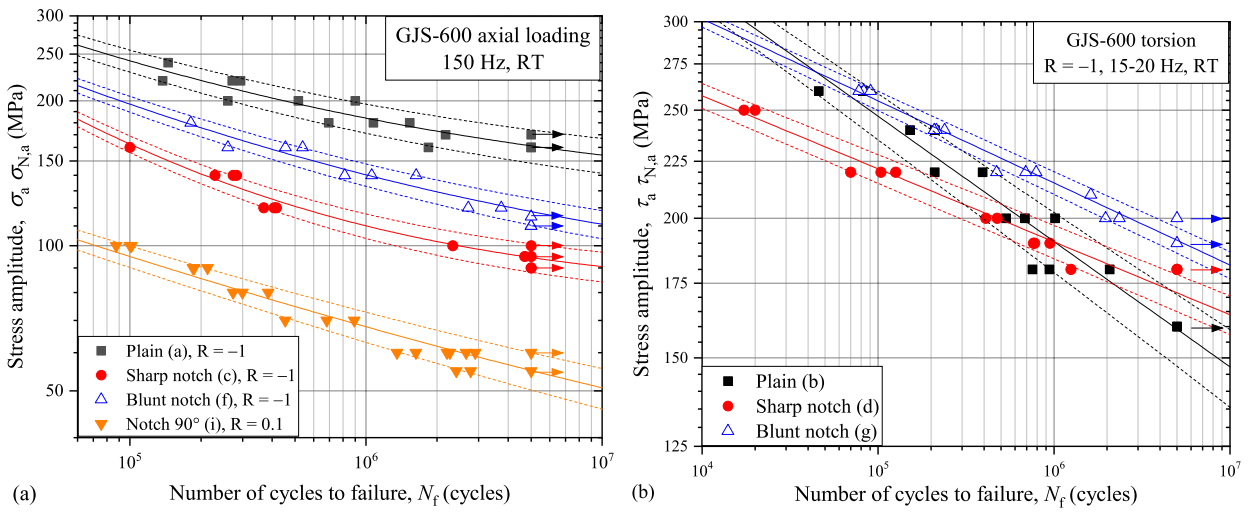
Figures

Figure 1. Geometry of the specimens used for the fatigue characterization. (a)-(b) plain, (c)-(i) notched specimens. (a), (c), (f), (i) used for axial fatigue tests, (b), (d), (e), (g), (h) for torsional and multiaxial fatigue tests. Dimension in mm. Fatigue data obtained from specimen geometries (c) and (f) were used to determine the mode I critical distance L^*, (d) and (g) to determine the mode III critical distance L_T^*.
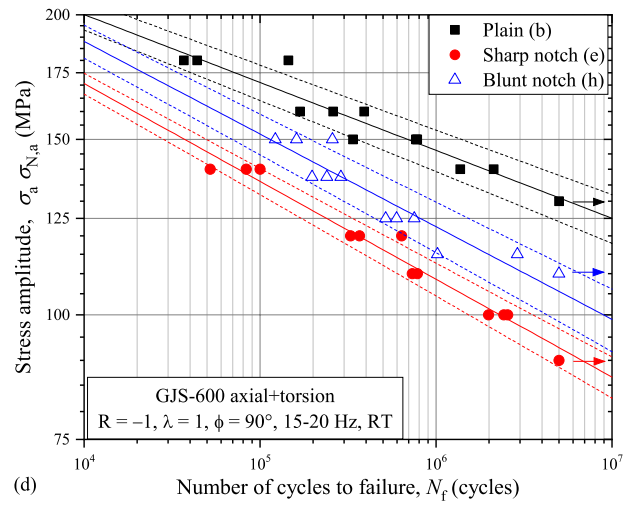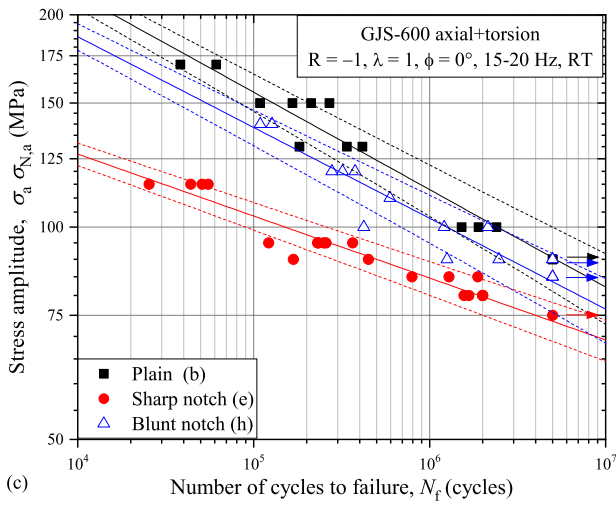
Figure 2. SN curves. Solid lines represent 50% failure probability, while dashed lines refer to 10% and 90% failure probability. Arrows indicated runout tests. (a) axial, (b) pure torsion, (c) in-phase combined axial and torsional, (d) out-of-phase combined axial and torsional fatigue tests.
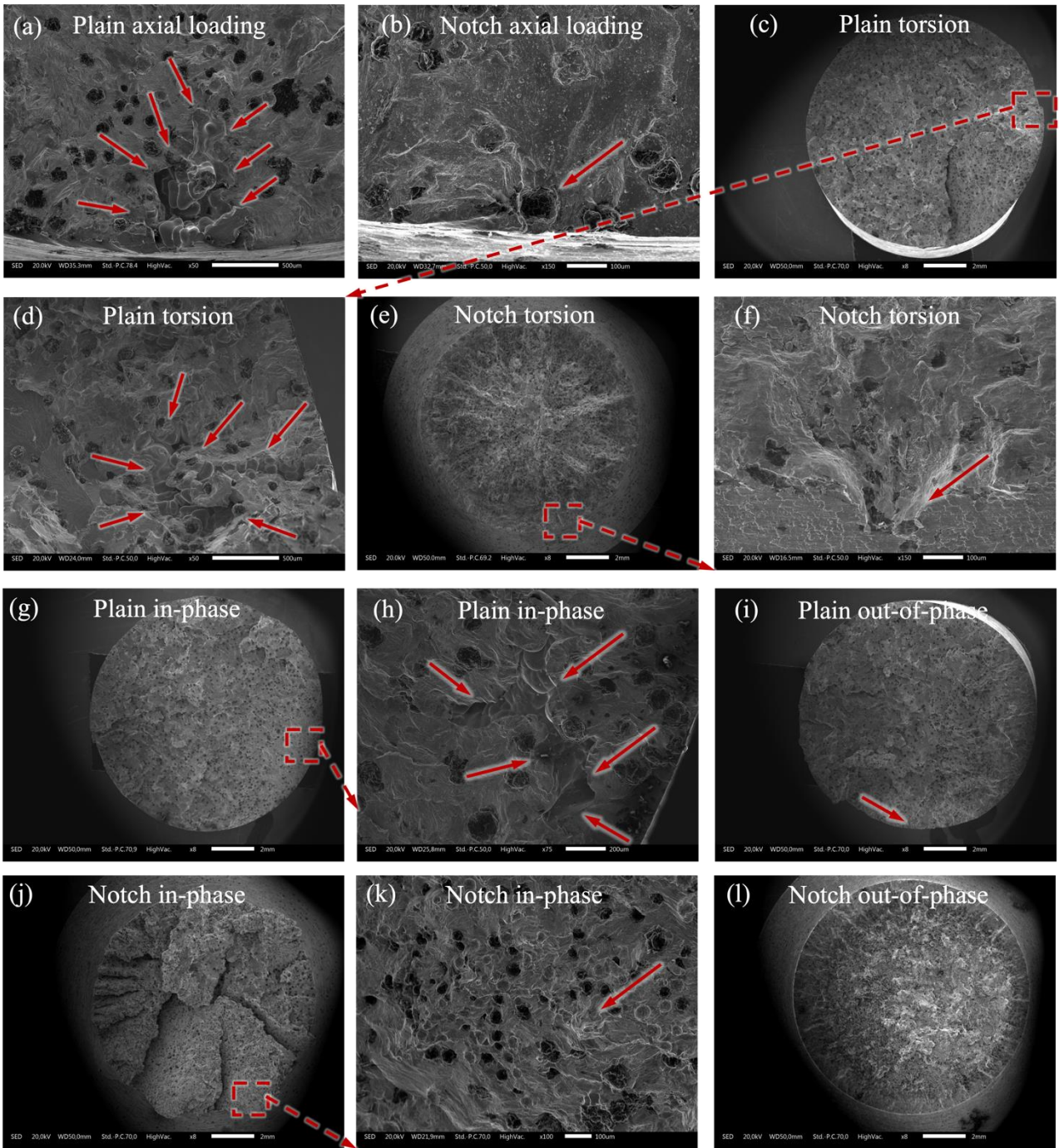
Figure 3. SEM micrographs of the fracture surfaces around the fatigue crack initiation site. The red arrows indicate the microshrinkage pore or the graphite nodule causing the crack initiation. (a) plain sample (a) under axial loading ($\sigma_a = 170$ MPa, $N_f = 2.1{\times}10^6$). (b) Fracture surface of a runout blunt-notched specimen (c) under axial loading ($\sigma_a = 110$ MPa, $N_f = 5{\times}10^6$) and then broken under tension-tension fatigue. (c) Overview and (d) detail of the fracture surface of a plain sample (b) tested under torsional loading ($\tau_a = 240$ MPa, $N_f = 2.1{\times}10^5$). (e) Overview and (f) detail of the fracture surface of a sharp-notched sample (d) tested under torsional loading ($\tau_a = 180$ MPa, $N_f = 6.5{\times}10^5$). (g) Overview and (h) detail of the fracture surface of a plain sample (b) tested under in-phase combined loading ($\sigma_a = \tau_a = 100$ MPa, $N_f = 1.9{\times}10^6$). (i) Overview of the fracture surface of a plain sample (b) tested under out-of-phase combined loading ($\sigma_a = \tau_a = 140$ MPa, $N_f = 2.1{\times}10^6$). (j) Overview

and (k) detail of the fracture surface of a sharp-notched sample (e) tested under in-phase combined loading (σ_a = τ_a = 85 MPa, N_f = 1.6 × 10⁶). (l) Overview of the fracture surface of a sharp-notched sample (e) tested under out-of-phase combined loading (σ_a = τ_a = 100 MPa, N_f = 2.4 × 10⁶).
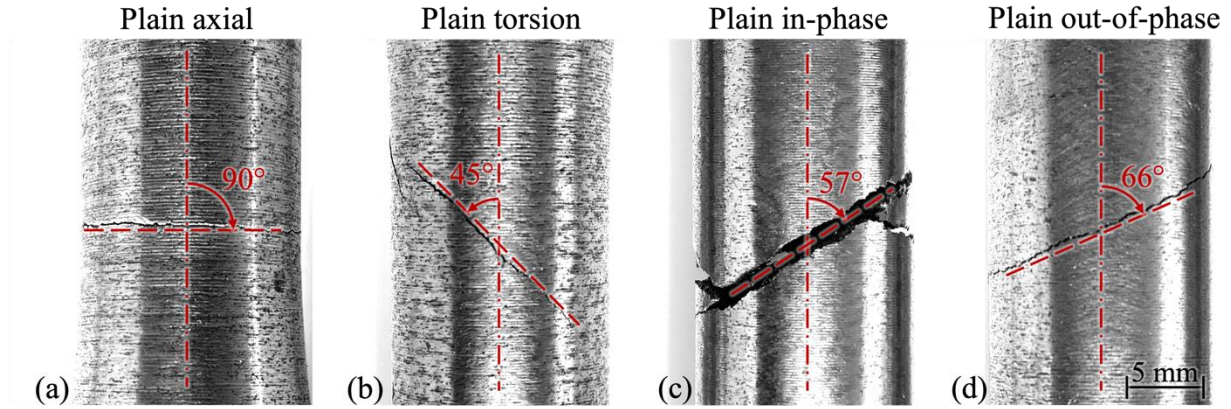

Figure 4. Optical micrographs of the crack path observed in the vicinity of the crack initiation site in plain samples tested under (a) axial (σ_a = 160 MPa, N_f = 1.8 × 10⁶), (b) torsional (τ_a = 180 MPa, N_f = 7.5 × 10⁵), (c) in-phase axial+torsional (σ_a = τ_a = 100 MPa, N_f = 1.9 × 10⁶), (d) out-of-phase axial+torsional loading (σ_a = τ_a = 140 MPa, N_f = 1.4 × 10⁶).
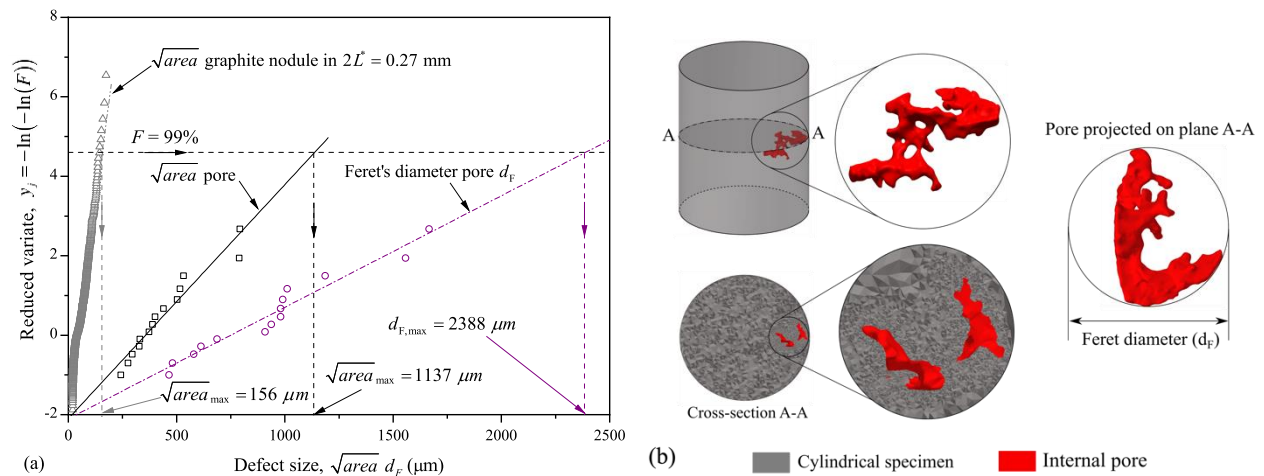

Figure 5. (a) Cumulative probability distributions of graphite nodules and shrinkage pores detected in [19] via CT scans. The analysis of graphite nodules is restricted to a toroidal volume centered on the notch tip and having radius equal to twice the critical distance of the material. The analysis of pores is performed on the whole scanned volume in terms of both square root of the projected area $\sqrt{area}$ and maximum Feret diameter d_F. (b) CT reconstruction of the largest pore found in the scanned specimen. The effect of the very irregular pore morphology on the fatigue strength is better captured by the Feret diameter d_F.
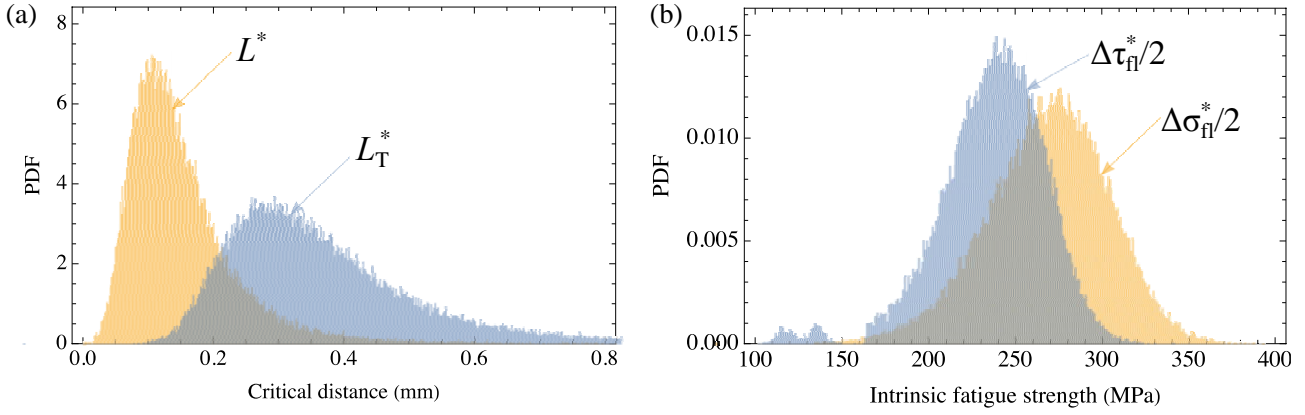
Figure 6. Histograms obtained from Monte Carlo simulations to assess the probability distribution function (PDF) of (a) the critical lengths L^*, L_T^* and (b) the intrinsic fatigue strengths $\Delta\sigma_{fl}^*, \Delta\tau_{fl}^*$ deduced from the double notch inversion methods devised in [19] and in the present paper for mode I and mode III loading, respectively.
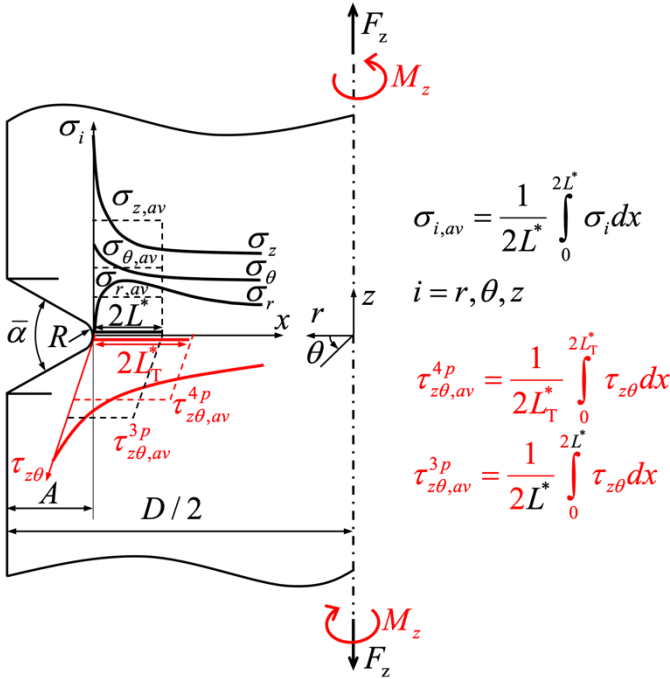

Figure 7. Schematic illustration of the TCD method applied in conjunction with a multiaxial fatigue criterion. Axial normal and torsional shear stresses are averaged along the notch bisector. In "4p" the average axial normal and torsional shear stresses are averaged along mode dependent critical distances, whereas in "3p" they are computed considering the same critical length.
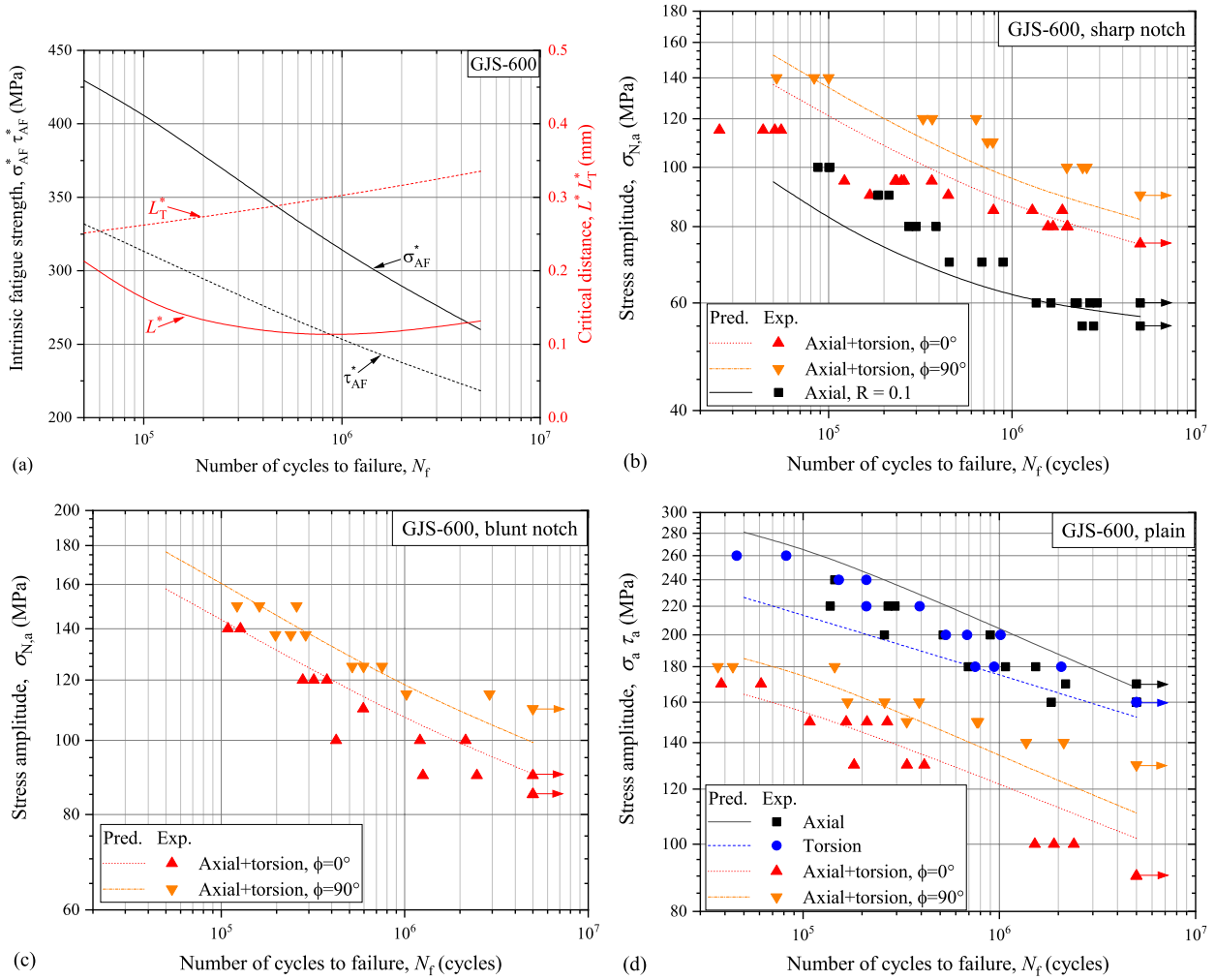
Figure 8. (a) Parameters σ_{AF}^*, τ_{AF}^*, L^*, L_T^* of the TCD+Carpinteri et al. multiaxial fatigue criterion assessed according to the double-notch inversion method as a function of the number of cycles to failure. (b), (c), (d) Prediction of the fatigue curves of independent plain, sharp- and blunt- notched variants, respectively, not used for the calibration of the TCD+multiaxial fatigue criterion.

Figure A.1. Determination of the critical distances for which the K_f ratio curves meet the experimental ones.

Tables

Table 1. Monotonic properties and Brinell hardness (based on four replicated tests). Standard error corresponds to 1σ uncertainty band.

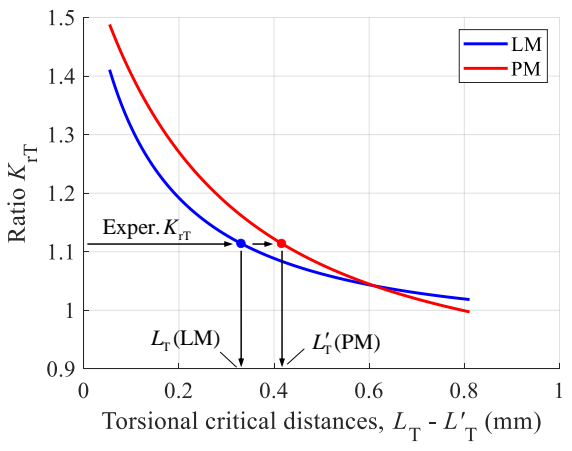| E (GPa)	G (GPa)	S_Y (MPa)	S_U (MPa)	T.E. (%)	HB
174±2	68.5±1.3	363±8	458±15	2.1±0.5	198±4
E: Young's modulus; G: elastic shear modulus; S_Y: 0.2% yield stress; S_U: ultimate tensile strength; T.E.: total elongation; HB: Brinell hardness					

Table 2. Notch root radius measured in the notched variants and corresponding stress concentration factor.

Specimen geometry	Notch root radius (mm)	Theoretical stress concentration factor K_t
Sharp Notch 60° R0.2 (c)	0.30±0.01	4.95 (axial)
Sharp Notch 60° R0.2 (d)	0.23±0.02	2.69 (torsional)
Sharp Notch 60° R0.2 (e)		5.61 (axial), 2.74 (torsional)
Blunt Notch 60° R1 (f)	1.00±0.01	2.87 (axial)
Blunt Notch 60° R1 (g)		1.68 (torsional)
Blunt Notch 60° R1 (h)		2.87 (axial), 1.69 (torsional)
Sharp Notch 90° R0.2 (i)	0.22±0.03	4.46 (axial)

Table 3. Best-fit coefficients of Eq. (1) used to interpolate the SN curves. S indicates the standard deviation. The high-cycle fatigue strength was assessed at 5×10^6 cycles.

Specimen geometry	type	Loading type	k_1 (MPa)	k_2 (MPa)	k_3	S (MPa)	$\Delta\sigma_{fl}/2,\ \Delta\sigma_{N,fl}/2$ $\Delta\tau_{fl}/2,\ \Delta\tau_{N,fl}/2$ at 5×10^6 cycles (MPa)
Plain	(a)	Axial, R = −1	123	3304.9	0.288	10	161
	(b)	Torsion, R = −1	-	899.20	0.112	9.2	159
	(b)	Axial+Torsion R = −1, λ = 1, ϕ = 0°	-	761.48	0.138	7.4	90.5
	(b)	Axial+Torsion R = −1, λ = 1, ϕ = 90°	-	374.78	0.068	5.5	131
Sharp Notch 60° R0.2	(c)	Axial, R = −1	79.2	12062	0.432	5.0	94.6
	(d)	Torsion, R = −1	-	470.29	0.065	5.1	172
	(e)	Axial+Torsion R = −1, λ = 1, ϕ = 0°	-	285.18	0.088	3.6	73.5
	(e)	Axial+Torsion R = −1, λ = 1, ϕ = 90°	-	421.60	0.098	3.2	92.7
	(f)	Axial, R = −1	78.2	2980.9	0.280	5.8	118
	(g)	Torsion, R = −1	-	593.91	0.073	3.9	191

Blunt Notch 60° R1 (c)	(h)	Axial+Torsion R = −1, λ = 1, φ = 0°	-	609.69	0.129	6.3	83.7
	(h)	Axial+Torsion R = −1, λ = 1, φ = 90°	-	442.71	0.093	5.5	106
Sharp Notch 90° R0.2 (d)	(i)	Axial, R = 0.1	21.0	722.99	0.198	3.8	55.1

Table 4. Results of the double-notch inversion method.

Loading type	Critical distance (mm)		Intrinsic fatigue strength (MPa)	
Axial	L^*	0.134	$\Delta\sigma_{fl}^*/2$	269.5
Torsional	L_T^*	0.333	$\Delta\tau_{fl}^*/2$	241.5

Table 5. Material parameters of the TCD+multiaxial fatigue criteria.

Criterion	Method	Parameter 1		Parameter 2		Critical distances	
		Symbol	Value	Symbol	Value	L^* (mm)	L_T^* (mm)
Fatemi-Socie	4p	α_{FS}^*	1.800	β_{FS}^*	3.506×10⁻³	0.0867	0.336
	3p		3.702		5.002×10⁻³	0.0953	0.0953
MWCM	4p	α_{MWCM}^* (MPa)	100.5	β_{MWCM}^* (MPa)	240.0	0.0841	0.300
	3p*		-		-	-	-
Carpinteri et al.	4p	σ_{AF}^* (MPa)	260.5	τ_{AF}^* (MPa)	218.3	0.131	0.336
	3p		316.0		316.0	0.121	0.121
Modified SWT	4p	α_{mSWT}^*	0.4956	β_{mSWT}^*	0.8467	0.130	0.337
	3p		0.6343		1.084	0.130	0.130
* No solution was found for the set of calibration equations							

Table 6. High- cycle fatigue strength predictions (5×10^6 cycles) for independent fatigue configurations.

Sample	Load	Exp.	Method	Fatemi-Socie		MWCM		Carpinteri et al.		Modified SWT	
				Pred.	Err. (%)	Pred.	Err. (%)	Pred.	Err. (%)	Pred.	Err. (%)
Blunt	Tors.	191	3p	226	18.4	-	-	214	11.8	217	13.6
Sharp	Ax. + Tors. φ=0°	73.5	4p	72.5	-1.31	61.6	-16.2	74.8	1.80	73.1	-0.53
			3p	61.7	-16.1	-	-	76.9 4.59		65.9	-10.3
Sharp	Ax. + Tors. φ=90°	92.7	4p	92.7	0.02	60.2	-35.1	82.3	-11.3	91.8	-0.93
			3p	92.6	-0.10	-	-	90.2 -2.71		102	9.71
Blunt	Ax. + Tors. φ=0°	83.7	4p	90.6	8.19	88.0	5.17	90.5	8.09	90.8	8.52
			3p	83.2	-0.54	-	-	98.5 17.7		91.8	9.73
Blunt	Ax. + Tors. φ=90°	106	4p	118	11.3	108	1.91	100	-6.06	118	11.3
			3p	118	11.3	-	-	114 7.70		118	11.3
Sharp 90°	Ax. R=0.1	55.1	4p	71.7	30.1	-87.0	-258*	57.0	3.48	63.4	15.1
			3p	68.3	24.0	-	-	58.0	5.20	74.1	34.5
Method				4p	3p	4p	3p**	4p	3p	4p	3p
Max abs. error (%)				30.1	24.0	258	-	11.3	17.7	15.1	34.5
RMS error (%)				13.1	14.7	75.7	-	6.39	9.7	8.46	17.3
* Condition set by Eq. (5b) is violated											
** No solution was found for the set of calibration equations											

Table 7. Prediction of plain fatigue strength according to Eq. (3).

F_{loc}				σ_W (MPa)

	S_U (MPa)	S_Y (MPa)	Exp. $\Delta\sigma_{fl}/2$ (MPa)	$d_{F,max} = 2388\ \mu m$	$\sqrt{area}_{max} = 1137\ \mu m$
1.41	458	363	161	164	186

Table 8. Carpinteri et al. criterion parameters for plain specimens (Eq. (8)) and predictions incorporating size dependent critical defect.

Parameters of Carpinteri et al. 4p model for plain samples			
σ_{AF} (MPa)		τ_{AF} (MPa)	
165.1		138.4	
Load	Exp.	Pred.	Err. (%)
Axial	161	168	4.34
Torsion	159	152	-4.40
Axial+Torsion $\phi = 0°$	90.5	102	12.7
Axial+Torsion $\phi = 90°$	131	111	-15.2
Max abs. error (%)		15.2	
RMS error (%)		10.4	